

SPH Simulation of a Twin-Fluid Atomizer Operating with a High Viscosity Liquid

G. Chaussonnet^{*,1}, S. Braun¹, L. Wieth¹, R. Koch¹, H.-J. Bauer¹
 A. Sanger^{2,3}, T. Jakobs², N. Djordjevic², T. Kolb^{2,3}

Karlsruher Institut fur Technologie (KIT), Karlsruhe, Germany

¹Institute of Thermal Turbomachines, KIT Campus South

²Institute of Technical Chemistry, KIT Campus North

³Engler-Bunte-Institute, KIT Campus South

*geoffroy.chaussonnet@kit.edu

Abstract

A Smooth Particles Hydrodynamics (SPH) 2D simulation of a twin-fluid atomizer is presented and compared with experiments in the context of bio-fuel production. The configuration consists in an axial high viscosity liquid jet ($\mu_l \approx 0.5$ Pa.s) atomized by a coflowing high-speed air stream ($u_g \approx 100$ m/s) at atmospheric conditions, and the experiment shows two types of jet instability (flapping or pulsating) depending on operating conditions and the nozzle geometry. In order to capture the 3D effects of the axial geometry with a 2D simulation, the surface tension force and the viscosity operator are modified. The mean and RMS velocity profiles of the single phase simulations show a good agreement with the experiment. For multiphase simulations, despite a qualitative good agreement, the type of instabilities as well as its frequency are rarely well captured, highlighting the limitation of 2D geometry in the prediction of 3D configurations.

Keywords: Numerical simulation, atomization, viscous fluids, air-assisted atomizer, SPH

Introduction

Recent predictions estimate the depletion of coal, oil and gas to year 2040, 2112 and 2042, respectively [1], which leaves approximately thirty years to find alternative and sustainable energy sources. The Bioliq[®] process (Fig. 1) proposes a solution based on the refinement of agricultural residuals, decoupled in two steps: (i) a decentralized stage where the biomass (mainly straw) is refined via fast pyrolysis in a compound of higher energy density called bioSyncrude[®], and (ii) a centralized stage that converts bioSyncrude[®] into synthetic gas (Syngas) at high temperature ($T_G \approx 1500^\circ C$) and pressure ($P_G = 80$ bars). Syngas is finally transformed to methanol, motor fuel [2] or even gas [3].

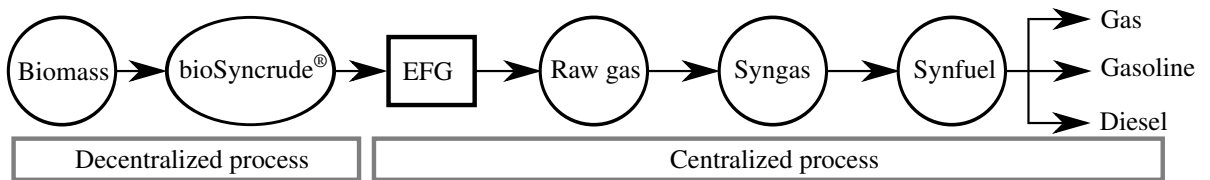


Figure 1 The Bioliq[®] process

At the first stage of the centralized process, bioSyncrude[®] is turned into a spray in a so-called Entrained Flow Gasifier [4] (EFG, depicted in Fig. 1) operating at P_G , through an air-assisted atomizer: the axial liquid jet of bioSyncrude[®] is sheared by a coaxial gas stream flowing at high velocity. Due to chemical equilibrium requirements, the Gas-to-Liquid Ratio (GLR), expressed as \dot{m}_g/\dot{m}_l , should be in the range 0.5 to 0.8 for a typical biomass based fuel, which limits the amount of atomizing material. In addition, the bioSyncrude[®] has a very large viscosity (≈ 10 Pa.s at low temperature in the low shear range) and a non-Newtonian behaviour. These constraints have a strong influence on the atomizing process, and the nozzle must be carefully designed in order to optimize the spray generation.

In this paper, the numerical simulation of a simplified nozzle supplied with a viscous Newtonian fluid is compared to experiments [5], in terms of gas velocity profiles and liquid instabilities frequency. The employed numerical approach is Smooth Particle Hydrodynamics (SPH), a method originally developed for astrophysics [6] and later adapted to free surface flow [7], especially when the gas phase can be neglected. In the field of air-assisted liquid atomization, the gas/liquid momentum transfer is the driving phenomenon so that both phases (of large density and viscosity ratio) must be accurately resolved. This particular context constitutes an original use of the SPH method

that was initiated by Höfler *et al.* [8, 9].

The experimental setup and its main observations are presented in the next part, followed by a description of the SPH method and the modifications added in this particular configuration. The results of the single phase and the multiphase 2D simulations will be presented in the fourth and fifth part, and a final conclusion will end the paper.

Experiment

In order to have a deeper insight into the atomization process occurring in the EFG, Sänger *et al.* [5] studied the fragmentation mechanism of a viscous fluid in a *twin-fluid external mixing atomizer* at atmospheric pressure and temperature conditions. It consists in an axial liquid jet sheared by a co-flowing high speed gas stream discharging into an open and quiescent atmosphere.

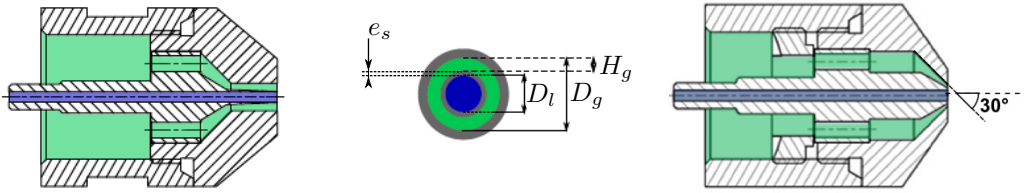


Figure 2 Schematics of external mixing twin fluid atomizer with parallel streams (*left*) and angle (*right*) nozzle. Geometrical parameters (*middle*) are detailed.

Two different nozzles were studied: (i) both gaseous and liquid streams are parallel (Fig. 2 *left*) and (ii) the gas stream has an incident angle of 30° (Fig. 2 *right*). In both configurations, the liquid diameter D_l and the gas height H_g are equal to 2 and 1.6 mm respectively. In the parallel configuration, the separator thickness e_s and the gas diameter D_g are equal to 0.1 and 5.4 mm respectively and to 0.5 and 6.2 mm in the angle configuration. Although several types of liquid were experimentally investigated, only two types of Newtonian liquid (L1 and L2) of different viscosity are discussed here. Their physical properties, as well as the gaseous ones, are summarized in Table 1.

Fluid type	Density ρ [kg/m ³]	Dyn. viscosity μ [Pa.s]	Surface tension σ [N/m]	Mass flow rate \dot{m} [kg/h]	Bulk velocity U [m/s]
L1	1233	0.2	0.0646	10	0.717
L2	1236	0.3	0.0643	10	0.713
Gas	1.2	$1.73 \cdot 10^{-5}$	-	4 - 8	54.9 - 107.8

Table 1 Physical properties of investigated fluids in atmospheric conditions.

The non-dimensional numbers that characterize this configuration are:

$$\text{Re} = \frac{D_h U}{\nu}, \quad \text{We} = \frac{\rho_g D_l U_{rel}^2}{\sigma}, \quad \text{Oh} = \frac{\mu_l}{\sqrt{D_l \rho_l \sigma}}, \quad \text{GLR} = \frac{\dot{m}_g}{\dot{m}_l}, \quad \text{M} = \frac{\rho_g U_g^2}{\rho_l U_l^2} \quad (1)$$

Equation (1) shows, in order of appearance: the Reynolds number where D_h is the hydraulic diameter equal to D_{liq} for the liquid and $2H_{gas}$ for the gas, the Weber number where U_{rel} is the liquid/gas relative velocity, the Ohnesorge number, the Gas-To-Liquid ratio, and the momentum flux ratio.

The test rig was instrumented with Laser Doppler Anemometry (LDA) for gaseous velocity measurement on vertical line at $x = 1.6$ and 1.4 mm for the parallel and angle nozzle respectively, and the liquid instabilities were recorded with a high-speed camera at a sampling frequency of 1200 Hz and with a pixel size of 143 μm . The time series were then post-processed by Proper Orthogonal Decomposition (POD) in order to extract the frequency and the wavelength of the instabilities. It was also observed that the jet undergoes different types of instability depending on the liquid viscosity and the GLR as illustrated in Fig. 3, leading to two different spray characteristics [5]. A pulsating mode is observed and consists in a longitudinal and axisymmetric mode triggered by a Kelvin-Helmholtz instability. Approximately five diameters downstream, the jet disrupts into a non-axisymmetric structure composed of bags and ligaments (Fig. 3a). A flapping mode is characterized by a deflection in the radial direction, in the early stage of the jet at approximately two diameters after the nozzle exit (Fig. 3b). The objective of the numerical simulation is to predict the onset of these modes at the right operating conditions.

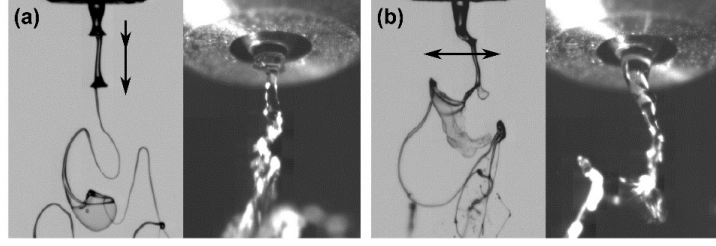


Figure 3 Side and oblique view of primary instabilities of a liquid jet with different dynamic viscosities at GLR = 0.4. (a) pulsating mode at $\mu_1 = 200$ mPa.s and (b) flapping mode at $\mu_1 = 300$ mPa.s, from [5]

Numerical Model

SPH Formalism

The SPH method is a mesh-free method that relies on a Lagrangian description of the fluid through particles moving at the fluid velocity and carrying physical properties such as mass, volume, momentum and energy. The starting point of the SPH discretization is the convolution of a field $f(\mathbf{r})$ by a Dirac function $\delta(\mathbf{r})$:

$$f(\mathbf{r}) = \int f(\mathbf{r}')\delta(\mathbf{r} - \mathbf{r}') d\mathbf{r}' \quad (2)$$

In order to apply Eq. (2) to discrete particles, the Dirac function is replaced by a smooth interpolation function $W(\mathbf{r} - \mathbf{r}', h)$ called the kernel and depicted in Fig. 4 (top). This function is defined on a compact support, the so-called *sphere of influence* that depends on the *smoothing length* h , and must fulfill mathematical properties such as the unity integral ($\int W(\mathbf{r} - \mathbf{r}', h) d\mathbf{r}' = 1$) and the convergence to δ when $h \rightarrow 0$. The kernel is chosen here as a quintic spline and $h = 3\Delta x$ where Δx is the mean particle spacing. The function f is thus expressed at the particle location \mathbf{r}_a by:

$$f(\mathbf{r}_a) = \sum_{b \in \Omega} V_b f(\mathbf{r}_b) W(\mathbf{r}_b - \mathbf{r}_a, h) \quad (3)$$

where V_b is the volume of particle b . The index b refers to neighbour particles located in Ω , the sphere of influence of the particle a , as illustrated in Fig. 4 (bottom). For the sake of clarity, in the following, $f(\mathbf{r}_a)$, $f(\mathbf{r}_b)$ and $W(\mathbf{r}_b - \mathbf{r}_a, h)$ are shortened to f_a , f_b and W_{ab} , respectively.

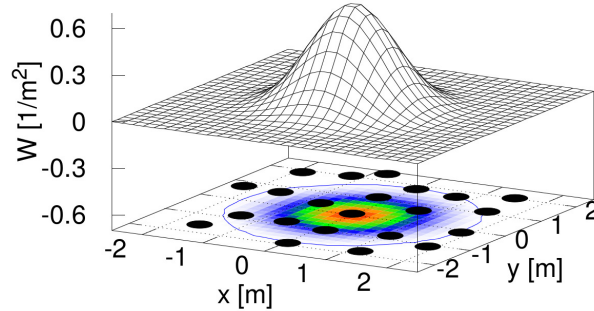


Figure 4 Bottom part: particle distribution superimposed with the kernel value and illustration of the sphere of influence. Top part: surface of a 2D kernel

The differential operators needed to evaluate the contact forces such as pressure, viscosity and surface tension are computed with the gradient of the kernel. The gradient [10] ∇f_a and the Laplacian [11] Δf_a are expressed as:

$$\nabla f_a = \sum_{b \in \Omega} V_b (f_b + f_a) \nabla W_{ab} \quad \text{and} \quad \Delta f_a = 2 \sum_{b \in \Omega} V_b (f_b - f_a) \frac{\partial W_{ab}}{\partial r} \quad (4)$$

Governing Equations

The Navier-Stokes equations are turned to a SPH form. The flow is considered isothermal so that the energy equation can be neglected. The continuity equation is solved algebraically by computing the particle volume and density:

$$V_a = 1 / \sum_{b \in \Omega} W_{ab} \quad \text{and} \quad \rho_a = m_a / V_a \quad (5)$$

where m_a is the constant mass of particle a . Equations (5) exactly conserve mass and as it relies only on the particle volume, the density expression avoids numerical diffusion of density near the liquid/gas interface. The momentum equation is given by:

$$\rho_a \left. \frac{d\mathbf{u}}{dt} \right|_a = \mathbf{f}_{a,p} + \mathbf{f}_{a,v} + \mathbf{f}_{a,st} \quad (6)$$

where \mathbf{u} is the particle velocity and the terms $\mathbf{f}_{p,a}$, $\mathbf{f}_{v,a}$ and $\mathbf{f}_{st,a}$ are the forces due to pressure, viscosity and surface tension, respectively. They write:

$$\mathbf{f}_{a,p} = - \sum_{b \in \Omega} V_b (p_b + p_a) \nabla W_{ab}, \quad \mathbf{f}_{a,v} = K \sum_{b \in \Omega} V_b \bar{\mu} \frac{\mathbf{u}_{ab} \cdot \mathbf{r}_{ab}}{r_{ab}^2 + \eta^2} \nabla W_{ab} \quad \text{and} \quad \mathbf{f}_{a,st} = -\sigma_a \kappa \delta_\Sigma \mathbf{n} \quad (7)$$

The expression of the pressure term conserves the linear momentum locally by ensuring $\mathbf{F}_{ab} = -\mathbf{F}_{ba}$ where $\mathbf{F}_{ab} = V_a V_b (p_b + p_a) \nabla W_{ab}$ is the elementary force that particle b exerts on particle a . Although the accuracy of this expression is significantly reduced by particle disorder [12], it artificially creates a term proportional to the background pressure that avoid "holes" of particle during the simulation.

The expression of the viscous term is a SPH form of the velocity Laplacian $\partial(\mu \partial \mathbf{u} / \partial \mathbf{x}) / \partial \mathbf{x}$. It exhibits the prefactor K equal to 8 in 2D [13], the inter-particle viscosity $\bar{\mu}$ deriving from a density-based average $\bar{\mu} = (\rho_a \mu_b + \rho_b \mu_a) / (\rho_a + \rho_b)$. It also involves the scalar product of velocity difference $\mathbf{u}_{ab} = \mathbf{u}_a - \mathbf{u}_b$ by the inter-particle distance vector $\mathbf{r}_{ab} = \mathbf{r}_a - \mathbf{r}_b$. The term $\eta = 0.1 h$ avoids the singularity when $r_{ab}^2 = 0$.

In the surface tension force, σ_a is the surface tension at particle a and κ is the interface curvature. The terms \mathbf{n} and δ_Σ are the interface normal and the surface-delta function, respectively, computed with the method proposed by Adami *et al.* [14].

To close the system, the pressure is expressed through a Tait state equation that depends on the particle density only:

$$p_a = \frac{\rho_0 c^2}{\gamma} \left[\left(\frac{\rho_a}{\rho_0} \right)^\gamma - 1 \right] + p_{back} \quad (8)$$

where ρ_0 is the nominal particle density and γ is the polytropic ratio that controls the *stiffness* of the pressure: due to the term $(\rho_a / \rho_0)^\gamma$, the pressure varies more intensively with regards to density variations when γ is larger. Note that γ intervenes directly in the compressibility β of the fluid, defined by $\beta = (\partial \rho / \partial p) / \rho$ at constant entropy: inverting Eq. (8) leads to $\beta = [\gamma(p - p_{back}) + \rho_0 c^2]^{-1}$ so the larger γ the lower the compressibility.

The term c in Eq. (8) is the fictive speed of sound and must be chosen to verify $c \geq 10 u_{max}$ in order to fulfill the weakly compressible condition by ensuring that density variation is lower than 1% [15], the final purpose being to increase the time step through the CFL condition. In the present configuration, the liquid and gaseous real Mach numbers are of different orders of magnitude, inducing different type of flow. With a velocity of the order of magnitude of 1 m/s, the liquid Mach number is $\approx 10^{-3}$ so that setting the fictive liquid speed of sound c_l to 50 m/s is appropriate. As a lower speed of sound increases the compressibility, it is necessary to increase γ for the liquid, so γ_l is set to 7. On the contrary, in the gas phase, the Mach number is ≈ 0.3 and the flow is compressible. The gaseous sound speed is therefore set to its real value (340 m/s in the experiment conditions) and γ_g is set to 1, so that Eq. (8) yields $p_{a,g} = c_g^2 (\rho_a - \rho_0) + p_{back}$.

Finally the background pressure p_{back} is added in Eq. (8) to ensure that pressure is always positive. Additionally, p_{back} controls the stiffness of the pressure gradient: rewriting Eq. (8) as $p = \delta p + p_{back}$ and injecting it in Eq. (7) leads to:

$$\mathbf{f}_{a,p} = - \sum_{b \in \Omega} V_b (\delta p_b + \delta p_a) \nabla W_{ab} - 2 p_{back} \sum_{b \in \Omega} V_b \nabla W_{ab} \quad (9)$$

where the second term of the RHS, proportional to p_{back} , is the artificial part of the pressure gradient that avoids holes formation in the lattice.

Three Dimensional Terms

As the simulations conducted in this paper are 2D, two modifications are added to the numerical method to represent the 3D effects of the experiment. First, in order to take into account the curvature of the round jet interface, an artificial surface tension force $\mathbf{f}_{a,curv}$ is added to the momentum equation:

$$\mathbf{f}_{a,curv} = -\epsilon_x \epsilon_y \frac{\sigma_a}{|y|} \delta_\Sigma \mathbf{n} \quad \text{with} \quad \epsilon_y = 1 - \exp\left(-\frac{y^2}{h^2}\right) \quad \text{and} \quad \epsilon_x = \left(1 - \frac{x}{L_c}\right)^{0.2} \quad (10)$$

where y is the radial coordinate and ϵ_y a damping function to avoid the singularity at $y = 0$. The function ϵ_x ensures that far from the nozzle, when the jet is fragmented in small droplets, the artificial surface tension force is

zero. It is defined between 0 and $L_c = 4 D_l$, and is equal to zero otherwise.

The second modification is to adapt the particularities of vectorial operators expressed in a cylindrical system to their Cartesian expressions, in order to take into account the divergence of the fields with y (r in the cylindrical system). The comparison between Cartesian (x, y) and cylindrical (r, z) coordinates show no difference for the gradient operator whereas the Laplacian differences yield, for the velocity:

$$\Delta_{CYL}(U_r) = \Delta_{CART}(U_y) + \frac{1}{y} \frac{\partial U_y}{\partial y} - \frac{U_y}{y^2} \quad (11)$$

$$\Delta_{CYL}(U_z) = \Delta_{CART}(U_x) + \frac{1}{y} \frac{\partial U_x}{\partial y} \quad (12)$$

The Laplacian operator, used for viscosity, is thus modified according to Eqs (11) and (12), the additional terms being also multiplied by ϵ_y (Eq. 10) to avoid the singularity at $y = 0$. Physically, these modifications render the difference of the shearing surface between the inner and the outer radius of an infinitesimal element. This difference is particularly significant at small radius (terms in "1/y").

Note that the modifications do not aim to model an axisymmetric domain but only the center slice of an axial configuration, so that it is not necessary to modify the computation of density.

Geometry and Boundary Conditions

The numerical domain depicted in Fig. 5 is composed of the inlet ducts and the cavity (length of 40 mm) where atomization takes place. The length of inlet ducts are seven diameters for the gas and three diameters for the liquid and the inlet velocity profiles are turbulent and laminar, respectively. A no-slip boundary condition is imposed at the walls of the inlets duct and the nozzle. In order to reproduce the entrainment rate \dot{Q}_e induced by the gaseous jets, the cavity is fed with a coaxial gas stream with a bulk velocity \bar{u}_e over a slit of height $H_e = 6.67$ mm. This ensures a proper entrained volume flow rate up to $x = 10$ mm such as $(\bar{u}_e H_e) = \dot{Q}_e(x=10 \text{ mm})$, and lead to $\bar{u}_e \approx 0.15 \bar{U}$. The restriction of the distance to 10 mm is to avoid a too large \bar{u}_e that could perturb the atomizing gas streams. On the sides of the cavity, the velocity is mainly axial due the entrainment flow, and the use of an outflow boundary condition would generate a strong numerical noise. Therefore, the cavity sides are set to slipping walls and they slightly open (semi-angle of 10°) to mimic the free jet opening after the nozzle. The outlet is set to a constant pressure equal to p_{back} .

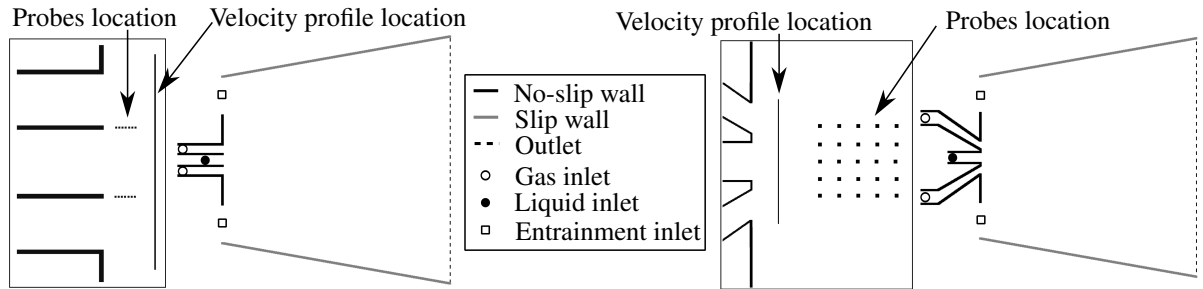


Figure 5 Sketch of the numerical domains and zoom on the nozzle exit. Left: parallel nozzle. Right: angle nozzle

Test Cases

Single-phase simulations assess for the accuracy of the SPH method when modeling low viscosity fluids such as air. Two different mass flows are tested on both nozzles. With the parallel nozzle, multiphase simulations are conducted to verify that 2D SPH can capture the pulsating mode at two different mass flows, and with the angle nozzle, the transition pulsating/flapping is studied by varying the gaseous mass flow and the liquid viscosity. All test cases are summarized in Table 2 where bold letters indicate how the case names are constructed.

Results and Discussion of Single-Phase Simulations

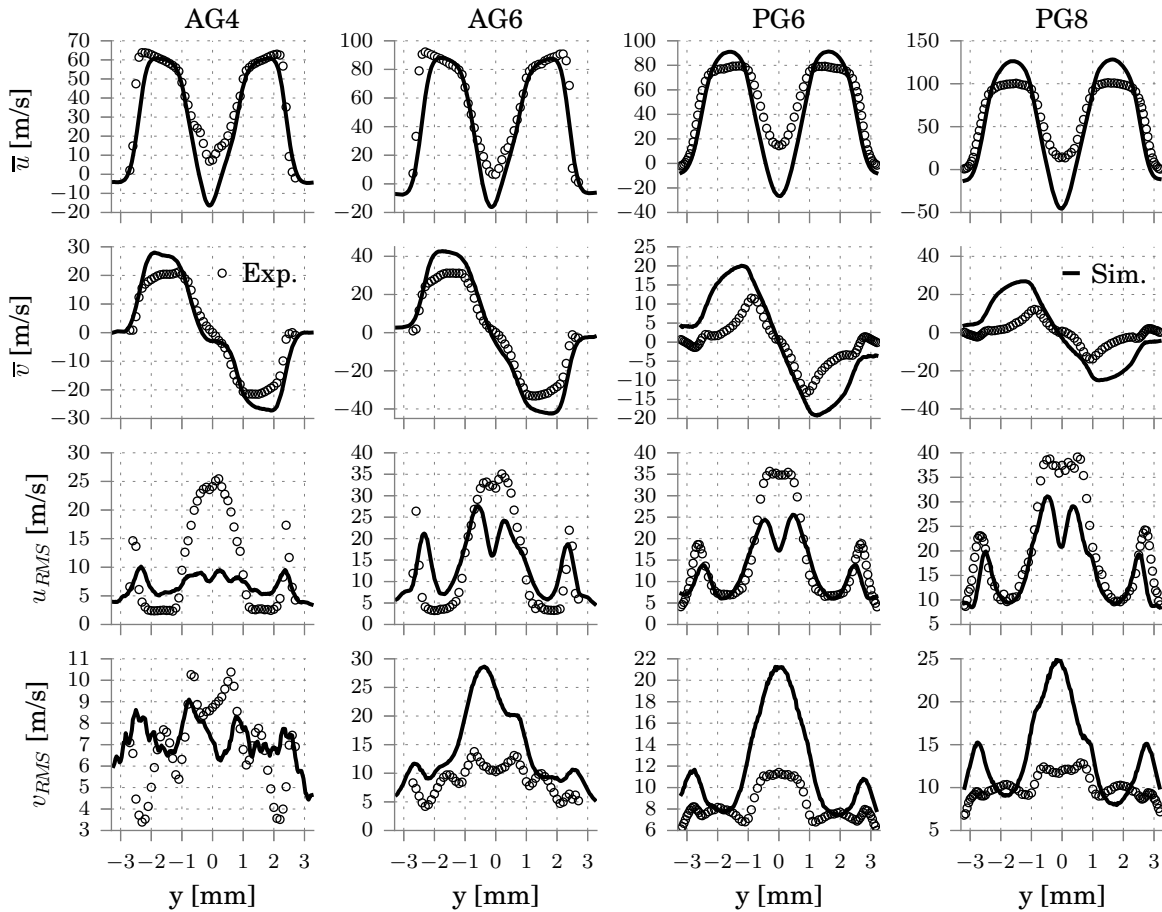
Figure 6 shows a velocity profile comparison, for the angle and parallel nozzle at two gaseous mass flow rates. The mean and RMS values are displayed for the axial (u) and radial (v) component. Note that as the radial component is Cartesian, it can have negative values. The simulations are averaged over 1000 snapshots regularly sampled over 18 convective times based on the cavity length.

Name	[-]	PG6	PG8	PL4	PL6	PL8	AG4	AG6	AL1M4	AL1M5	AL1M6	AL2M4	AL2M5	AL2M6
Nozzle	[-]	PAR	PAR	PAR	PAR	PAR	ANG	ANG	ANG	ANG	ANG	ANG	ANG	ANG
Liq. type	[-]	Gas	Gas	L1	L1	L1	Gas	Gas	L1	L1	L1	L2	L2	L2
\dot{m}_g	[kg/h]	6	8	4	6	8	4	6	4	5	6	4	5	6
U_g	[m/s]	81.9	107.8	54.9	81.9	107.8	54.9	81.9	54.9	68.5	81.9	54.9	68.5	81.9
GLR	[-]	-	-	0.4	0.6	0.8	-	-	0.4	0.5	0.6	0.4	0.5	0.6
Re_g	[$\times 1000$]	18.3	24.1	12.3	18.3	24.1	12.3	18.3	12.3	15.3	18.3	12.3	15.3	18.3
We	[-]	-	-	175	393	684	-	-	175	274	393	176	274	395
M	[-]	-	-	5.72	12.7	22.1	-	-	5.72	8.91	12.74	5.76	8.96	12.81

Table 2 Test-case matrix

For the angle nozzle, the mean values are in good agreement with the experiment for the two mass flows but (i) \bar{u} shows a too smooth profile, possibly due to the lack of turbulence model, and (ii) the extrema of \bar{v} are slightly over-predicted, resulting in too opened jet. The predicted u_{RMS} show peaks at the right y position but they are smoother than experimental results, highlighting more widespread fluctuations. The model cannot capture the central peak, probably due to the too large jet opening. The radial RMS velocity is slightly unsymmetrical and predicts a too large peak in the center for AG6. The same comments are valid for the parallel nozzle with the difference that (i) \bar{u} extrema are slightly over-predicted, (ii) the jet is even more opened and (iii) u_{RMS} is predicted with the right intensity, except for the central peak.

Concerning the axial velocity, the good predictions of its mean and the acceptable levels of its RMS in the air


Figure 6 Mean and RMS profiles of axial and radial velocity, at $x = 1.6$ mm and 1.4 mm for the parallel and angle nozzle, respectively. Experiment: \circ , simulation: $-$

stream region ensure that the gas will shear the liquid with the right average and fluctuating intensity. As the radial velocity is more difficult to capture, it can be expected that the dynamic pressure felt by the liquid interface ($\rho_g v^2$)

will slightly deviate from reality, especially in terms of fluctuations, possibly leading to an earlier destabilization of the jet.

Results and Discussion of Multiphase Simulations

Table 3 summarizes the instability modes observed in experiment and simulation. For the parallel nozzle, the simulation capture a transition between a *sinusoidal* pulsating mode (phase shift $\varphi = \pi$ between top and bottom probes) and a flapping mode, while experiments only show a *varicose* pulsating mode ($\varphi = 0$). Cases PL4 and PL6 can be compared to the experiment in terms of frequency while PL8 simulation is purely flapping. With the angle nozzle and liquid L1, experiment show a pulsating mode while simulations only predict a flapping mode, preventing further quantitative comparisons. With the liquid L2, flapping modes in both the experiment and the simulation are observed, but with an opposite trend with increasing gas velocity. Nevertheless, a quantitative comparison is achieved for L2 in the following.

Case	PL4	PL6	PL8	AL1M4	AL1M5	AL1M6	AL2M4	AL2M5	AL2M6
Exp.	Puls.	Puls.	Puls.	Puls.	Puls.	Puls.	Flap.	Flap.	Puls./Flap.
Sim.	Puls.	Puls./Flap	Flap.	Flap.	Flap.	Flap.	Puls./Flap.	Flap.	Flap.

Table 3 Observation of instability modes

Figure 7 compares experimental and simulated time series, for one case of each geometry. For PL6 (Fig. 7a-c), similar structures are observed: a central liquid core right after injection of length $\approx 2D_l$ that further disrupts into finer ligaments. However the time series of PL6 shows a behaviour closer to flapping than pulsating, and the second *instability stage* (p_1) is tilted due to flapping while it remains axially oriented in the experiment. In addition, when the liquid bubble bursts (bag breakup), the atomized droplets are ejected axially in the experiment whereas radially in the simulation, due to the flapping motion (arrow in Fig. 7c). The AL2M5 case (Fig. 7d-f) shows a proper flapping mode with a predicted flapping frequency qualitatively close to the experiment. In this configuration, the second stage of the liquid core (p_2 and p_3) is tilted in the simulation.

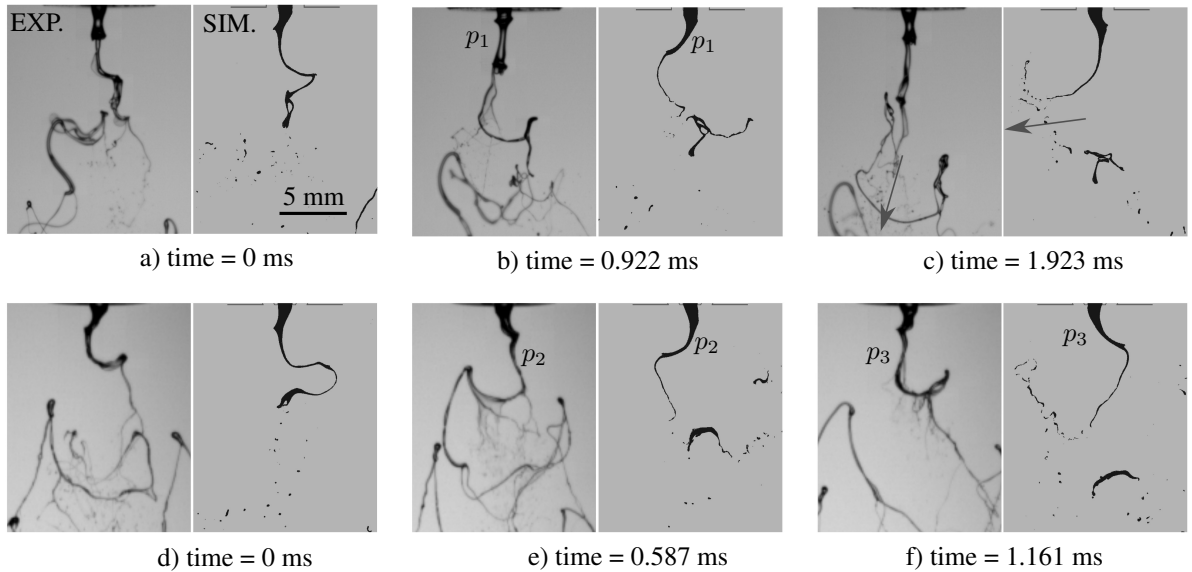


Figure 7 Comparison of experiment/simulation time series for PL6 (a,b,c) and AL2M5 (d,e,f)

Figures 8a and 8b depict the frequency f versus the gas mass flow rate, for the pulsating mode with the parallel nozzle (a) and for the flapping mode with the angle nozzle with liquid L2 (b). Experimentally, the frequencies were calculated by POD while in the simulation, they were computed from probes recording the liquid presence at the location defined in Fig. 5. Several interspectra were computed via FFT and the frequency of largest intensity was kept. The error bars in Fig. 8 correspond to the frequency resolution of the FFT. For the parallel nozzle (Fig. 8a), the frequency f_p increases with the gas mass flow rate as in experiments, but the linearity ($f_p \propto \dot{m}$) is not recovered, and two points may be not sufficient to endorse the validity of the present linear regression. With the angle nozzle (Fig. 8b), the trend is also recovered but the linear regression does not show a purely proportional dependency, due to a non-zero y -intercept ($y = ax + b$ with $b \neq 0$). Figure 8c shows the velocity u_c of the wave

propagation on the interface directly downstream the injection and the associated wave length λ for PL6. The velocity u_c is computed by measuring the time difference Δt between two consecutive probes separated by Δx . The velocity is then $\Delta x/\Delta t$ and the wavelength λ is equal to the ratio of the velocity by the peak frequency f_p according to $\lambda = u_c/f_p$. The prediction of u_c shows an appropriate order of magnitude but its dependence on \dot{m} is not clearly defined due to a strong uncertainty, while λ is acceptably predicted with PL4 and underpredicted for PL6.

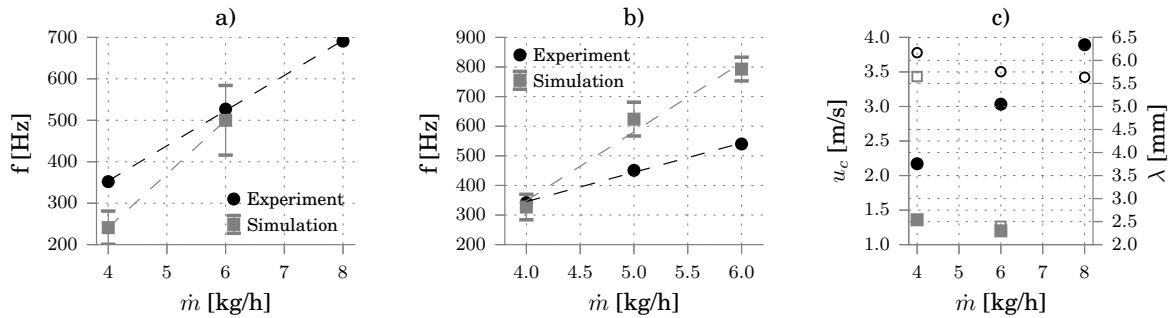


Figure 8 Comparison of experiment/simulation, a) pulsating frequency with the parallel nozzle, b) flapping frequency with the angle nozzle and L2. On plot c), ● and ■ represent u_c for experiment and simulation respectively, while ○ and □ represents λ for experiment and simulation respectively.

Conclusion

The 2D numerical simulation of a twin fluid atomizer with SPH method showed that the gaseous flow was acceptably predicted on a two-dimensional domain, in terms of mean and RMS velocity profile. When considering the multiphase configuration, the simplified 2D approach has shown strong limitations, despite the 3D modifications of the surface tension force and the viscosity. This emphasizes that in this particular configuration of air-assisted atomization, the prediction of an appropriate gaseous shear stress is not sufficient to guarantee a proper liquid behaviour. The modes of instability are not well captured and predictions even show an inverted pulsating/flapping transition with gas mass flow rate in case of angle nozzle with liquid L2. However when simulations and experiments have the same mode, the time series show a qualitatively good agreement in terms of shape and structure of the ligament, and the predicted frequencies have comparable values with the experiment. Finally the wave velocities and the associated wavelengths show the right order of magnitude but the trends are not well captured. In the optic of accurately capturing the transition of instability modes and their associated values (frequency and wavelength) with SPH method, it is thus necessary to compute a 3D domain.

Acknowledgement

This work was performed on the computational resource ForHLR Phase I funded by the Ministry of Science, Research and the Arts Baden-Württemberg and DFG ("Deutsche Forschungsgemeinschaft").

References

- [1] Shafiee, S. and Topal, E., *Energy Policy*, 37(1):181 – 189 (2009).
- [2] Dahmen, N.; Dinjus, E.; Kolb, T.; Arnold, U.; Leibold, H. and Stahl, R., *Environmental Progress & Sustainable Energy*, 31(2):176–181 (2012).
- [3] Dahmen, N.; Dinjus, E. and Henrich, E., *Oil Gas European Magazine*, 33(1):31 (2007).
- [4] Higan, C. and Van der Burgt, M., *Gasification*, Gulf professional publishing (2011).
- [5] Sanger, A.; Jakobs, T.; Djordjevic, N. and Kolb, T., *ILASS Europe* (2014).
- [6] Gingold, R. and Monaghan, J., *Monthly Notices of the Royal Astronomical Society*, 181:375 – 389 (1977).
- [7] Monaghan, J. and Kocharyan, A., *Computer Physics Communications*, 87:225 – 235 (1995).
- [8] Hofler, C.; Braun, S.; Koch, R. and Bauer, H.-J., *ILASS - Europe 2011, 24th European Conference on Liquid Atomization and Spray Systems, Estoril, Portugal, September 2011* (2011).
- [9] Hofler, C.; Braun, S.; Koch, R. and Bauer, H.-J., *Proceedings of ASME Turbo Expo 2012* (2012).
- [10] Monaghan, J., *Reports on Progress in Physics*, 68:1703 – 1759 (2005).
- [11] Cleary, P. and Monaghan, J., *Journal of Computational Physics*, 148:227 – 264 (1999).
- [12] Chaussonet, G.; Braun, S.; Wieth, L.; Koch, R. and Bauer, H.-J., *Proceedings of 10th SPHERIC International Workshop* (2015).
- [13] Macia, F.; Antuono, M.; Gonzalez, L. M. and Colagrossi, A., *Progress of theoretical physics*, 125(6):1091–1121 (2011).
- [14] Adami, S.; Hu, X. and Adams, N., *Journal of Computational Physics*, 229:5011 – 5021 (2010).
- [15] Monaghan, J., *Journal of Computational Physics*, 110:399 – 406 (1994).